



Water Saturation Effects on Thermal Infrared Radiation Features of Rock Materials During Deformation and Fracturing

Xin Cai¹ · Zilong Zhou¹ · Lihai Tan¹ · Haizhi Zang^{1,2} · Zhengyang Song³

Received: 25 November 2019 / Accepted: 19 June 2020 / Published online: 30 June 2020
© Springer-Verlag GmbH Austria, part of Springer Nature 2020

Abstract

This paper aims to investigate the water saturation effects on the thermal infrared radiation (IRR) characteristics of rock materials during deformation and fracturing processes. Three kinds of rocks, namely sandstone, granite, and marble, were adopted for tests. Uniaxial compression tests were carried out on oven-dried and water-saturated rock samples. The evolution of IRR temperature on rock surface was monitored and recorded with the aid of an infrared thermographic camera. Test results show that the IRR temperature of saturated samples is apparently higher than that of dry ones subjected to the same axial stress. After water saturation, the heating rate in elastic deformation phase, the IRR temperature increment at peak stress, and the IRR temperature on the new-formed fracture surface have a significant growth compared to dry condition. These indicate that the presence of water facilitates the release of thermal energy. The sensitivities of the heating rates in elastic deformation phase to water saturation are very distinct for the three rocks. This is possibly resulted from the mineral composition of rock types, especially the proportion of calcite and swelling clay minerals. The IRR temperature increment at peak stress for rock not only depends on the moisture condition, but is also relevant to the uniaxial compressive strength.

Keyword Thermal infrared radiation · Water saturation · Average infrared radiation temperature · Coupling thermal-elastic effect · Rock fracture

Abbreviations

IRR	Infrared radiation
AIRT	Average infrared radiation temperature
ΔT	Variation in average infrared radiation temperature
ZOI	Zone of interest
AE	Acoustic emission
UCS	Uniaxial compressive strength
W_e	Radiant energy intensity
ϵ	The emissivity of the object

α	Stefan–Boltzmann constant
T	Absolute infrared radiation temperature
σ	Uniaxial stress
ΔT_f	AIRT increment at peak stress
ΔT_{\max}	The maximum temperature increment

1 Introduction

Every object exposed to a temperature above absolute zero will emit electromagnetic radiation with a large range of wave lengths (Fig. 1), such as radiofrequency radiation, microwave radiation, infrared radiation (IRR), and light radiation (Brady and Rowell 1986; Martelli et al. 1989; Wu et al. 2000). Among them, the IRR waves fall in the electromagnetic spectrum within wavelengths ranging between 0.7 and 1000 μm , in which the portions within the length of 2.5–15 μm possess the thermal effect. Therefore, the IRR is also popularly known as “heat radiation”. The IRR waves are invisible to human eyes but visually traceable by specific infrared detectors. Due to its non-destructive and non-contact nature, high sensitivity, and space visibility, the IRR detection is widely employed in industrial, engineering,

✉ Xin Cai
xincai@csu.edu.cn

✉ Zilong Zhou
zizhou@csu.edu.cn

¹ School of Resources and Safety Engineering, Central South University, Changsha 410010, China

² ARC Centre of Excellence for Geotechnical Science and Engineering, Faculty of Engineering and Built Environment, The University of Newcastle, Callaghan 2308, Australia

³ Geotechnical Institute, TU Bergakademie Freiberg, Gustav-Zeuner-Straße 1, 09599 Freiberg, Germany

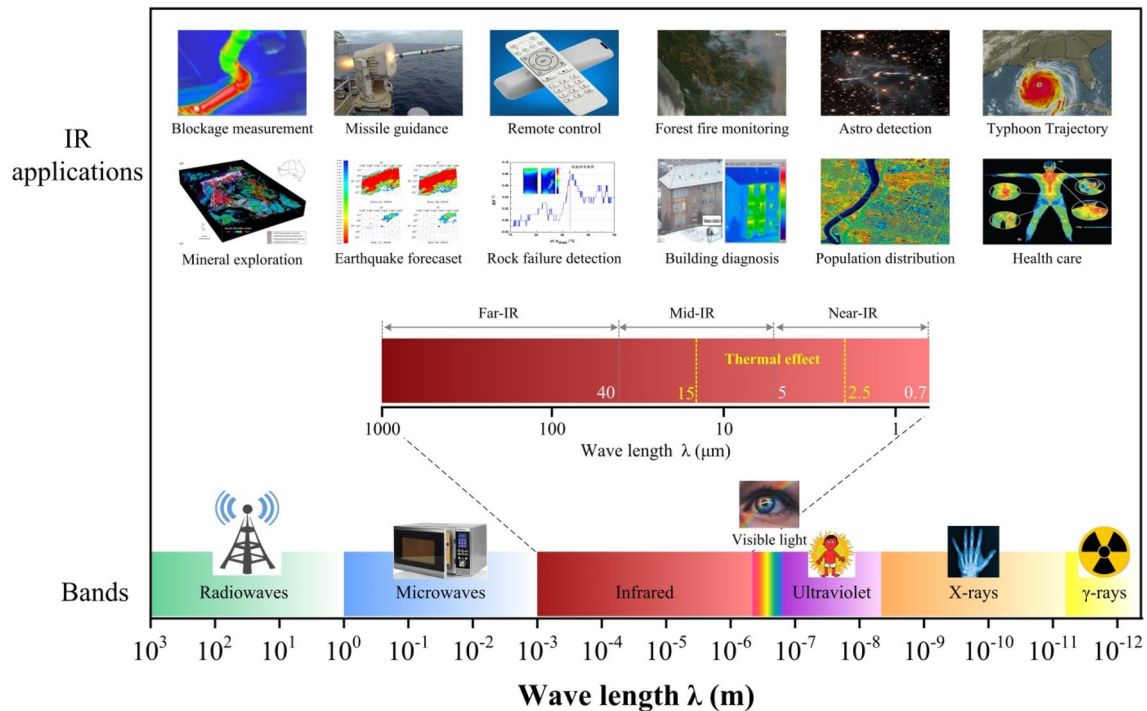


Fig. 1 Electromagnetic spectrum of infrared region and applications of infrared radiation technology

military, and medical sectors (Yao et al. 2013; Cong et al. 2016; Ren et al. 2019). Particularly in the applications of rock engineering, it proves to be an effective approach for remote sensing, such as landslides (Pappalardo et al. 2018), rock burst (Sun et al. 2017b), pillar degradation (Seo et al. 2017), tunnel excavation (He et al. 2010; Sun et al. 2017b), and earthquakes (Saraf et al. 2008). An in-depth and comprehensive understanding of the IRR features of rock materials during deformation and fracturing processes is indispensable to monitor and forecast the natural and human-induced hazards.

To date, the investigations on the thermal infrared radiation characteristics have been conducted on various types of rocks, including sandstone (Wu and Wang 1998; Wu et al. 2006a, b; Du et al. 2015; Sun et al. 2017b; Cheng et al. 2018; Ma et al. 2019c), marble (Wu et al. 2002, 2004, 2006a, b), granite (Wu et al. 2002, 2006a, b) Luong and Emami 2013; Du et al. 2015; Salami et al. 2017; Liu et al. 2018), limestone (Liu et al. 2006; Wu et al. 2006a, b; Wang et al. 2016; Salami et al. 2017), coal (Wu and Wang 1998; Wu et al. 2006a, b; Zhao and Jiang 2010; Ma et al. 2013, 2016; Sun et al. 2017a; Li et al. 2018; Ma and Sun 2018; Xiao et al. 2019), shale (Salami et al. 2017), gabbro (Zheng et al. 2017), basalt (Mineo and Pappalardo 2016, 2019), and concrete (Minh Phono Luong 1990; Zhang et al. 2012; Lou and He 2018). Concretely speaking, Minh Phono Luong (1990) first used the infrared thermographic camera to detect the initiation and development of micro-cracks in rock and concrete

samples under uniaxial and fatigue loadings. In the first decade of this century, Wu et al. (2000) made significant contributions to the remote-sensing rock mechanics based on thermal IRR thermographic technique. They detected the temperature both on surface and inside the rock using an IRR thermographic camera and thermal-sensitive sensors, respectively. Their test results demonstrates that the temperature measured inside the rock shows the similar trend with respect to the surface IRR temperature. In addition, Wu et al. (2002) investigated the variations of the average infrared radiation temperature (AIRT) for uniaxial loaded marble and granite samples. They reported that the AIRT rises with the increase of applied stress. They also documented that both of rock type and failure pattern can impact the maximum value of AIRT. Afterwards, Wu et al. (2006a, b) conducted a bunch of tests on various types of rock to study the IRR properties of rock. They obtained the spatiotemporal evolution laws of rocks, respectively, subjected to uniaxial compression, and shear and tension stresses. It is suggested that the abrupt changes of the AIRT-time curve and the IRR image can be used as the precursors for rock fracturing. Sun et al. (2017a) proposed an innovative approach to eliminate the background thermal noise using two controlled samples. Sun et al. (2017b) also observed the evolution of IRR temperature field in rock burst tests. It is documented that the AIRT of sample drops obviously and abnormal bands appear before the occurrence of rock burst. More detailed information concerning the IRR characteristics of rock-like

materials under deformation is summarized in Table 1. It is widely shared that compression and shear loads lead to the increase of IRR temperature, while the tensile stress results in a temperature reduction.

However, the above-mentioned experimental studies have been limited to dry state. As known to all, water is one of the most crucial and relevant environmental factors controlling rock properties. For in-situ conditions, rock masses are commonly exposed to wet condition in essence, due to the rain, seepage, underground water, and even damp air (Zhou et al. 2018a; Ma et al. 2019a; Cai et al. 2020). Thus, it is highly worthwhile to investigate the effects of water saturation on the IRR behavior of rocks. Moreover, previous research documented that water weakens the rock strength and stiffness (Hawkins and McConnell 1992; Yang et al. 2013; Jiang et al. 2014; Zhou et al. 2016, 2018a, 2019; Zhao et al. 2017; Tang et al. 2018; Wasantha et al. 2018; Bian et al. 2019; Cai et al. 2019, 2020; Weng et al. 2019; Yao et al. 2019; Jia et al. 2019; Liu et al. 2019a; Dang et al. 2019). The loss extent of strength and stiffness is strongly dependent on rock types (Wong et al. 2016; Cai et al. 2019). Whether water shows a pronounced and distinctive impact on the IRR behavior for different rock types is still not quite clear. The IRR characteristics sensitivity to water for different rock types should be revealed in a more detailed manner.

The primary objective of this study is to explore the effects of water saturation on IRR characteristics of rocks as well as the water sensitivity of IRR behavior for different rock types. Three typical rocks were adopted for tests. Uniaxial compression tests were conducted on rock samples under oven-dried and water-saturated conditions to determine the mechanical properties. Meanwhile, the IRR temperature evolution on rock surface was detected and recorded by an infrared thermographic camera. Some important IRR parameters, such as the heating rate in elastic deformation phase, the temperature increment at peak stress, and the maximum temperature on fracture surface before failure, were analyzed.

2 Test Materials and Methods

2.1 Material Characterization and Sample Preparation

Three types of rock commonly encountered in rock engineering were selected for tests, i.e., sandstone, granite, and marble. Figure 2 presents optical polarized micrographs of the three rocks. Their mineral compositions and corresponding grain sizes are listed in Table 2. Table 3 illustrates some essential physical parameters. More detailed descriptions about the three rocks can be referred to our previous publications (Cai et al. 2019).

For each rock type, all samples were obtained from one rock block without visible geological weakness to minimize the scatters of the physical properties across the sample sets. Samples were first sliced into $50 \times 50 \times 100$ mm³ rectangular prisms, and then, six surfaces of each sample were grinded to be smooth and parallel. The ultrasonic wave velocity was measured to collect samples with similar physical properties (Song et al. 2018). Ten samples for each rock type (a total of 30 samples) were used for tests. After that, all samples were placed in a vacuum oven at 105 °C for more than 48 h for the purpose of complete water evaporation.

To determine the immersion time for water saturation, a preliminary immersion test was performed. Three dry rock samples (one for each rock type) were first submerged in purified water for free soaking, and then, they were taken out and weighed every hour until their masses remain unchanged. The continual variations of water content against immersion time for the three rock samples are shown in Fig. 3. It can be clearly observed that the water content of samples remains unchanged in 24 h. Then, the samples are regarded as reaching the completely saturated state. Hereby, half of rock samples were immersed in water for more than 24 h for full saturation in this study.

2.2 Experimental Set-Up

Uniaxial compression tests were conducted using an electric servo-hydraulic material testing machine (INSTRON 1346) installed at the Advanced Research Center at Central South University (see Fig. 4). The displacement rate was controlled at 0.24 mm/min for all tests, i.e., the sample was tested with a constant strain rate of 4×10^{-5} /s.

An uncooled infrared thermographic camera (SC7000 FLIR) was applied to detect the IRR temperature evolution during the loading process. This camera can detect the infrared radiation for the wavelengths ranging from 3.7 to 4.8 μ m with the temperature sensitivity of 0.01 °C. It was operated to capture the IRR images with 112×194 pixel resolution for a 62×108 mm² actual area at a 100 Hz frame rate. In tests, the IR camera was placed at a secure distance (1.0 m) from the sample to avoid the damage and disturbance caused by the flying rock fragments. Specific measures were adopted to minimize the environmental impact on the IRR temperature detection as follows: (1) the samples were placed in the laboratory at least 24 h before tests to have the same temperature with the environment; (2) the sample and infrared thermographic camera were placed in a cuboid aluminum isolation box to prevent disturbances from outside, such as light, air motion, and radiation from other objectives; (3) black paint was sprayed on the inner surfaces in the aluminum box to avoid the light reflection by aluminum plates. Additionally, prior studies suggested that the region selected for temperature analysis should be

Table 1 Summary of experimental studies on the IRR features of rock-like materials

Authors	Material	Loading condition	IR thermographic camera model	Precision (°C)	Wave length (μm)	Sample rate (fps)	Important findings
Minh Phono Luong (1990)	Concrete	UC, CC	AGA-782 Thermalvision	0.1	3.6–5.5	25	IRR thermography can detect the crack initiation and coalescence
Wu and Wang (1998)	Rock salt	UC, CC	AGA-782 Thermalvision	0.1	3.6–5.5	25	(1) Local stress concentration causes local high IRR (2) Lower T ₁ strip forecasts the crack position;
Wu et al. (2002)	Coal	UC, CC	AGA-782 Thermalvision	0.025	N.A	N.A	(1) AIRT increases with rock deformation (2) Rock type and failure pattern affects the IRR properties
Wu et al. (2004)	Sandstone	UC	TVS-8100 MKII	0.025	N.A	60	The velocity of projectile is quadratically related to the ΔAIRT of sample
Wu et al. (2006a)	Marble	PI	TVS-8100 MK II	0.025	2.5–3.5	N.A	The spatial-temporal evolution of IRR on rock surface can forecast the rock failure
Wu et al. (2006b)	Various rocks	UC, CS, BC, BS, PI	N.A	N.A	N.A	N.A	(1) Three AIRT precursors for rock failure: short dropping; fast rising and dropping to rising (2) AIRT precursors for rock failure occur at 77–94% of corresponding rock strength
Liu et al. (2006)	Various rocks	UC, CS, BC	N.A	N.A	N.A	N.A	(1) ΔAIRT is affected by loading condition: PI > CS > UC > 3 PB (2) The IRR during rock failure is primarily controlled by the frictional heat effect
Wu et al. (2006)	Marble	UC, CS, PI; 3 PB	TVS-8100 MK II	0.025	3.6–4.6	1	(1) ΔAIRT is affected by loading condition: PI > CS > UC > 3 PB (2) The IRR during rock failure is primarily controlled by the frictional heat effect
Gabbro							
Limestone							
Granodiorite							
Zhao and Jiang (2010)	Coal	UC, CC	IR913A	0.06	8–14	50	(1) Selected region for AIRT analysis should be close to the sample center (2) For normal coal under UC, the AIRT failure precursor occurs at 0.79 σ _c . However, precursors appear at 0.9σ _c and 0.82σ _c for bump-prone coal under UC and CC conditions, respectively
Sheinin and Blokhin (2012)	Rock salt	UC	RTN-31	N.A	N.A	N.A	The deformation period can be identified by using IRR data
Zhang et al. (2012)	Concrete	UC	CAMTM SC3000	0.02	7.5–13	N.A	Water seepage causes a sudden drop of AIRT
Luong and Emami (2013)	Diorite	CC	N.A	N.A	3–5	N.A	IRR technology reveals the damage mechanism by stress concentration in weakness zones
Granite							
Du et al. (2015)	Granite	TU	ThermoView P120	N.A	N.A	N.A	T distribution on rock surface is affected by failure modes
Sandstone							
Ma et al. (2016)	Coal	UC	FLIR A615	<0.05	7.5–14	25	The VIRT of OIIS and the VIRT of SMIIS are applicable for rock failure detection
Wang et al. (2016)	Limestone	UC	InfRec R300	0.05	8–14	4	(1) The turning point of AIRT from dropping to rising again occurring at 89.5%σ _c is the key point for predicting rock failure (2) Abnormal trips appear in the central region of sample before failure

Table 1 (continued)

Authors	Material	Loading condition	IR thermographic camera model	Precision (°C)	Wave length (μm)	Sample rate (fps)	Important findings
Salami et al. (2017)	Limestone Granite Shale Mortar	BD	Jade MWIR	0.1	N.A	500	(1) AIRTs of BD disk rock samples decrease with the load (2) For three rocks, the temperature rises suddenly around the crack. However, that for mortar samples does not change apparently (3) The difference in AIRT is induced by the mineralogy of rock materials The BTNC method is proposed to improve the signal/noise ratio of AIRT
Sun et al. (2017a)	Coal	UC	FLIR A615	<0.05	7.5–14	25	(1) AIRT increases rapidly in plastic period (2) Before rock burst, AIRT apparently drops and anomaly bands occur (3) The main frequency of AE decreases during test
Sun et al. (2017b)	Sandstone	TU	ImageIR4325	0.025	3.7–4.8	N.A	Using VOIIS and VSMIIS curves, precursors of upcoming failure and initial failure for coal occur at 86.3–98.0% of σ_c and 60.4–91.9% of σ_c , respectively
Ma and Sun (2018)	Coal	UC	FLIR A615	<0.05	7.5–14	25	The inclination of pre-fabricated fissure affects the IRR characteristics of rock. With the increasing inclination, the AIRT increases firstly and then decreases. The maximum value of AIRT occurs at the fissure inclination of 60°
Cheng et al. (2018)	Sandstone	UC	Optris PI450	N.A	7.5–13	10	(1) The AIRT of saturated rock is higher than that of dry one (2) The failure precursor of saturated rock is easier identified by the minimum T curve (3) The fluctuation in AIRT of saturated sample is more obvious
Liu et al. (2018)	Granite	UC	InfraTec Image IR8325	N.A	3.7–4.8	80	(4) For saturated sample, the T at the left and right sides of increases during rock burst, while that decreases for dry one
Li et al. (2018)	Coal	UC	N.A	N.A	N.A	N.A	The IRRT of coal is affected by gas pressure
Lou and He (2018)	Concrete	UC	Optris PI450 Fluke TiS	N.A N.A	7.5–13 7.5–14	10 1	(1) The IRRT distribution follows Gaussian distribution (2) The obvious drop point in R ² -time curve can be considered as a precursor for rock failure (3) The spatial IRRT field coincides with the stress field similar to the hyperbolic paraboloid

UC uniaxial compression, CC cyclic compression, PI projectile impact, CS coupled compression-shear, BC biaxial compression, BS bi-shear, 3 PB three-point bending, TU triaxial unloading, σ_c uniaxial compressive strength, IRR infrared radiation, T temperature, IRRT infrared radiation temperature, $\Delta AIRT$ average infrared radiation temperature, $\Delta AIRT$ increment in average infrared radiation temperature, VIRT variance of infrared radiation temperature, OIIS original infrared image sequences, VOIIS variance of original infrared image sequences, SMIIS successive minus infrared image sequences, VSMIIS variance of successive minus infrared image sequences, BTNC background thermal noise correction, R² the goodness of Gaussian fitting, N.A. data not available in the reference

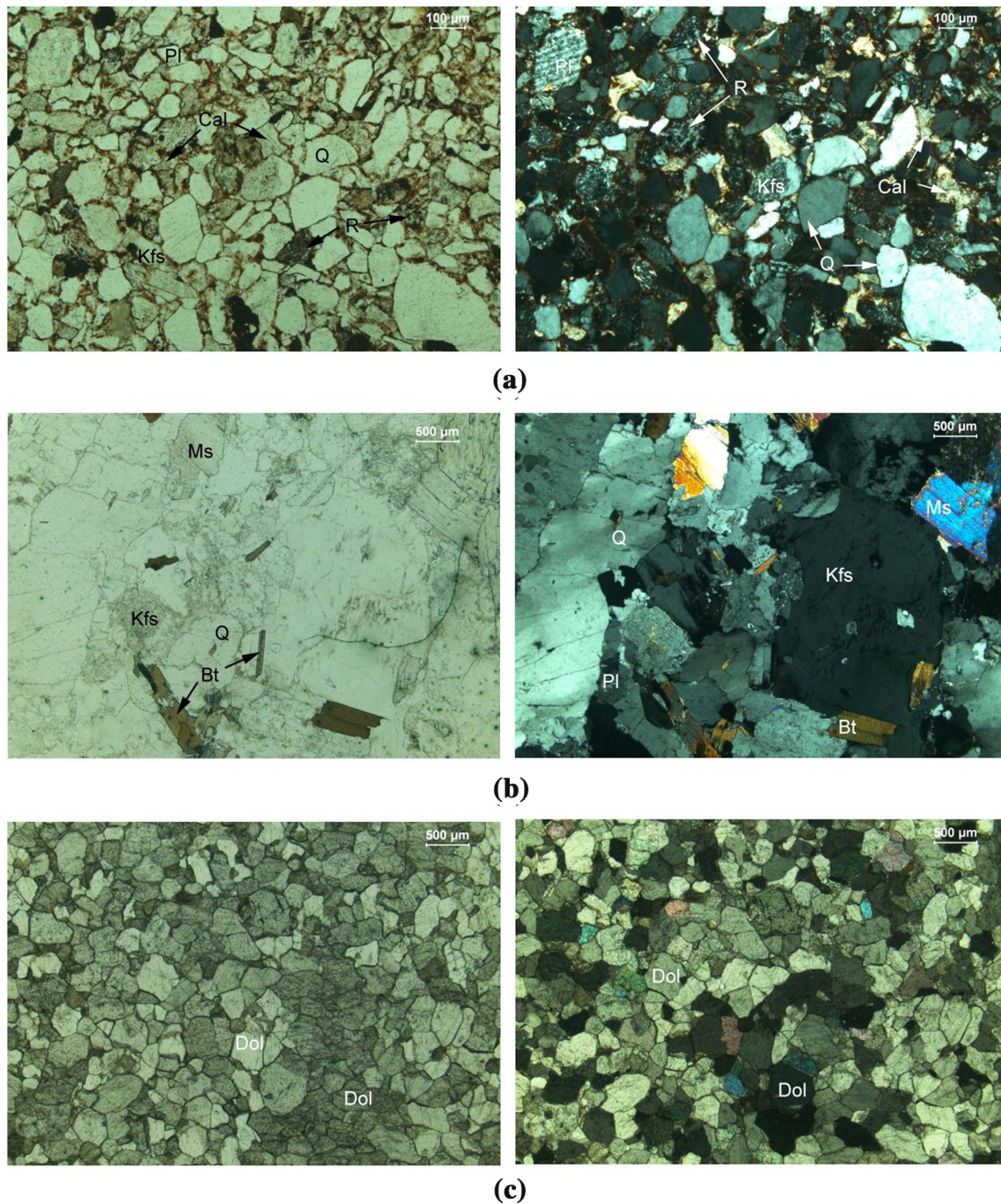


Fig. 2 Optical plane-polarized (left) and cross-polarized (right) micrographs of **a** sandstone, **b** granite, and **c** marble (*Q* quartz, *Kfs* kalium feldspar, *Pl* plagioclase, *R* rock debris, *Ms* Muscovite, *Bt* biotite, *Dol* Dolomite)

near the sample center which is more sensitive to temperature variation (Zhao and Jiang 2010; Wang et al. 2016). In this paper, we computed the variations of average infrared radiation temperature (ΔT) in a zone of interest (ZOI) with 84×100 pixel resolution in the sample center, as shown in Fig. 5, to represent the global temperature change on the sample surface.

The rock sample also emits acoustic waves due to deformation or damage in tests. The acoustic waves can be detected by the acoustic emission (AE) sensors and then converted into electrical signals, so that they can be recorded. In recent years, the AE signals are widely used to assess the damage condition inside rock (Zhou et al. 2018b; Ma et al. 2019b; Song et al. 2020; Zhang et al. 2020) and locate any defects (Zhou et al.

Table 2 Percentage and grain size of mineralogical compositions for three rock types (Cai et al. 2019)

Rock type	Mineral composition	Percentage % ^a	Grain size ^b /mm	Average grain size / μm
Sandstone	Quartz	57.20	0.02–0.25	0.055
	Feldspar	13.48	0.05–0.24	
	Calcite	5.26	0.01–0.15	
	Mica	3.84	0.04–0.14	
	Smectite	9.72	0.01–0.03	
	Chlorite	4.05	0.01–0.05	
Granite	Feldspar	38.77	0.1–2.5	1.970
	Quartz	32.82	0.2–2.2	
	Muscovite	22.85	0.05–2.2	
	Chlorite	5.56	0.01–0.2	
Marble	Dolomite	96.98	0.1–0.6	0.083
	Calcite	3.02	0.1–0.4	

^aThe percentage of mineral compositions was determined by X-ray diffraction technique

^bThe grain size is measured by optical micrographs

Table 3 Some essential physical parameters of the tested rocks

Rock type	P %	ρ / $\text{kg}\cdot\text{m}^3$	A_w %	C_p / $\text{m}\cdot\text{s}^{-1}$
Sandstone	8.50	2368.5	2.29	3094.0
Granite	1.07	2620.3	0.52	4333.4
Marble	0.63	2821.2	0.13	5241.5

P porosity, ρ density, A_w water absorption, C_p primary wave velocity

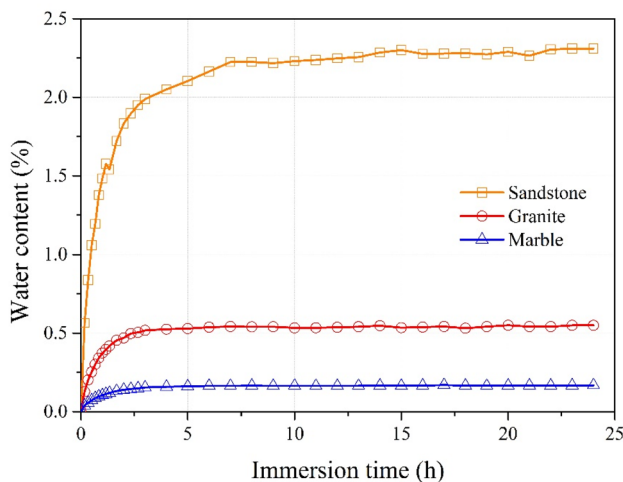


Fig. 3 Variation of water content versus immersion time

2020). In the present study, the AE technique was applied to monitor and record the AE counts to facilitate the analysis of crack initiation and evolution. Two AE sensors (Nano 30) and pre-amplifiers (PAC 2/4/6) were used. A threshold value of 45 dB was set to eliminate the potential noises. During whole testing process, the room temperature was kept at 25 °C and the humidity is controlled at 60% by air conditioner to minimize the data discreteness.

2.3 Principle of Thermal Infrared Radiation Detection

An object emits electromagnetic radiation with a large range of wavelengths, in which only the IRR band has the thermal effect. In the infrared thermographic camera, a germanium lens with the specific refraction coefficient can separate the IRR wave from all categories of electromagnetic radiation (see Fig. 5), which indicates that only the IRR waves can be captured by the camera. Subsequently, the radiant energy of IRR waves is received by the focal plane array detector element and then transformed into temperature information according to the Stefan–Boltzmann law (Boltzmann 1884):

$$W_e = \epsilon \alpha T^4, \tag{1}$$

where W_e is the radiant energy intensity; ϵ is the emissivity of the object, for a blackbody, $\epsilon = 1$, for a graybody, $0 < \epsilon < 1$; $\alpha = 5.6696 \times 10^{-8} \text{W}/(\text{m}^2 \cdot \text{K}^4)$ is the Stefan-Boltzmann constant; T is the absolute temperature of the object (K). The output IRR image shows the surface energy intensity map.

Rocks are typically porous-elastic-plastic. Under external stresses, the deformation and fracture of rock will alter its internal energy and trigger energy transition into IRR energy. Hence, the variation of IRR temperature can, to a certain extent, characterize the stress state of rock. The temperature evolution of rock during loading process is dominated by coupled thermo-mechanical effects (Minh Phono Luong 1990; Wu et al. 2006b; Luong 2007), including pore gas escaping, thermal-elastic effect, fracture effect, frictional heat effect, and heat conduction effect.

3 Test Results and Discussion

In this section, we analyze and discuss the experimental results of different rock types in oven-dried and water-saturated states under the following five sub-sections.

3.1 Water-Induced Changes in Mechanical Properties

Table 4 displays the average values of the mechanical properties, including uniaxial compressive strength (UCS), elastic modulus, and critical strain, of the three rock types. All

the three mechanical properties are deteriorated by water. The loss extent of these parameters was determined accordingly and is shown in Fig. 6. It can be observed from Fig. 6

that the water-induced reductions in the UCS for the three rocks are markedly distinct. Among the three rock types, the sandstone has undergone the largest decline in UCS, up to

Fig. 4 Photographic view of experimental setup

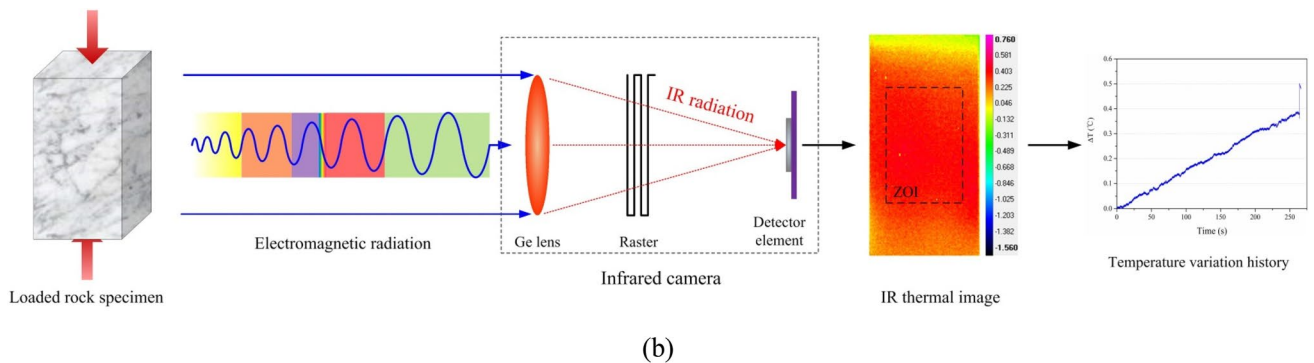
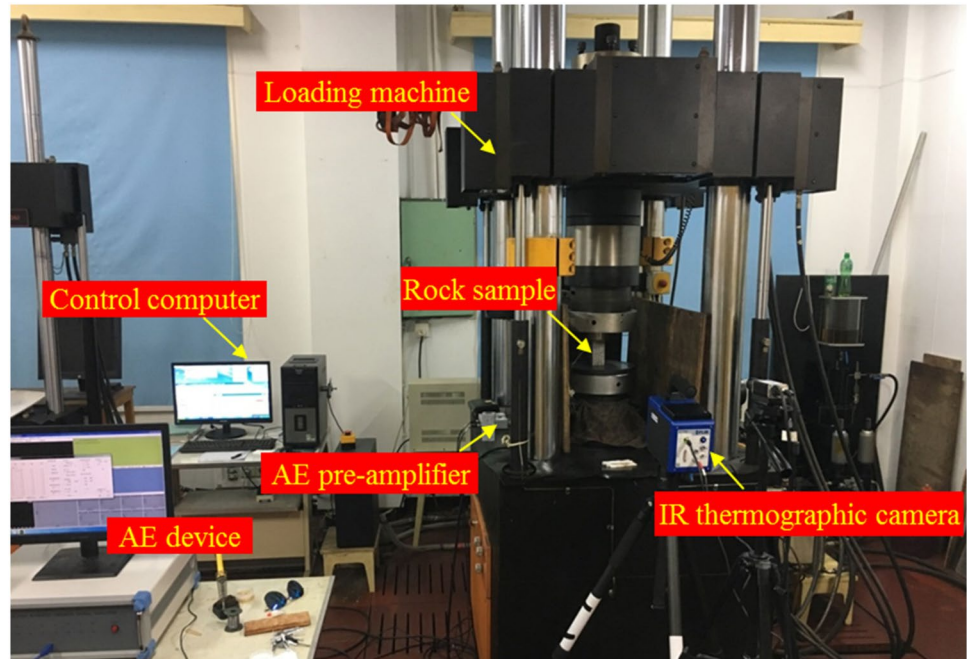


Fig. 5 Schematic view for infrared thermographic technology (*Ge* germanium, *ZOI* zone of interest)

Table 4 Average test results of rocks under dry and saturated conditions

Rock type	State	t_f /s	σ_c /MPa	E /GPa	ϵ_c /‰	N_c /10 ³	a /°C·MPa ⁻¹	ΔT_f /°C	ΔT_{max} /°C
Sandstone	Dry	253.0	71.91	7.05	10.21	18.0	2.8	0.236	0.615
	Sat	225.9	50.48	5.52	9.16	3.7	6.2	0.409	0.949
Granite	Dry	216.6	123.82	15.18	8.46	985.7	2.7	0.361	1.469
	Sat	204.8	119.39	14.34	8.32	184.5	4.1	0.570	2.029
Marble	Dry	174.0	119.48	16.82	7.12	8.1	2.0	0.299	0.908
	Sat	176.5	118.77	16.78	7.08	5.9	3.9	0.640	1.846

t_f time-to-failure, σ_c uniaxial compressive strength, E elastic modulus, ϵ_c critical strain, N_c cumulative AE counts, a heating rate during elastic deformation phase, ΔT_f the variation of AIRT on rock surface at peak stress, ΔT_{max} the maximum temperature increment on the new-formed fracture surface

29.8%. The UCS of the granite slightly dwindles by 3.58% after water saturation. However, an approximately negligible UCS loss for the marble is observed, indicating that the UCS of the marble is not apparently affected by water. In addition, the elastic modulus and critical strain follow a similar weakening pattern as for UCS. Under water-saturated condition, the elastic modulus and critical strain of the sandstone display the most drastic drop; however, for the granite, these parameters only undergo a relatively gentle dip while the marble exhibits the least loss in terms of the two properties. The water-weakening mechanisms are not discussed herein, since we have elucidated the reasons in the previous publication (Cai et al. 2019).

3.2 Relationship Between the Variation in Surface Temperature, Uniaxial Stress, and AE Counts

Figure 7 demonstrates the histories of axial stress, AE counts, and the variations of AIRT (ΔT) versus time for each rock type under dry and saturated conditions. Evidently, the evolution manner of AE counts is similar for all samples regardless of moisture condition and rock types. According to the slope of stress and the occurrence of ring counts, loading history can be divided into four phases. In each phase, the evolution characteristics of the AIRT variation are as follows:

1. Crack closure phase (phase I): where initial defects (such as pores and micro-cracks) are closed (Peng et al. 2019), and quite limited AE counts occur. At the start of loading, the temperature variation of dry rocks may be negative, accompanying drastic fluctuation. This behavior is particularly obvious for the dry sandstone. This is likely due to the shrink of volume and the pore breaking, gases

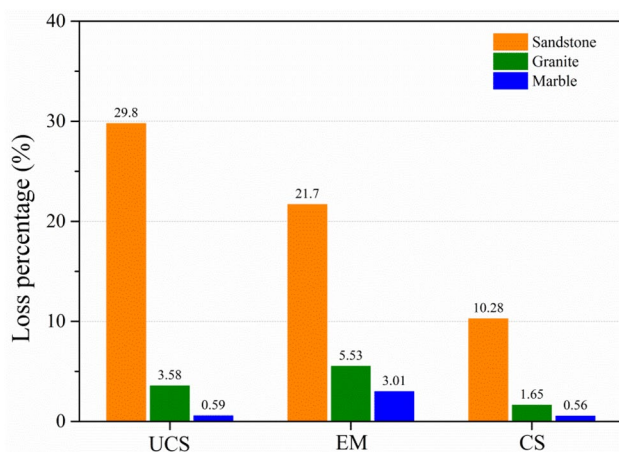


Fig. 6 Loss percentage of mechanical properties of three rock types due to water saturation (*UCS* uniaxial compressive strength, *EM* elastic modulus, *CS* critical strain)

(e.g., CO_2 , O_2 , and SO_2) primordially enclosed in pore escape and take the heat away. Theoretically, the more porosity or absorbed gases, the more the IRR temperature reduction as well as the more violent fluctuation (Wu et al. 2006b). However, for saturated samples, water occupies the majority of pore spaces instead of gases, the heat loss induced by the escape of pore gases is limited. Hence, the AIRT variation of the three rocks rises at the loading initiation.

2. Elastic deformation phase (phase II): where rock samples deform elastically and micro-cracks initiate steadily. The axial stress on the samples increases fast. The AIRT of rocks continues to rise due to the thermal-elastic effect. This will be analyzed in the next section.
3. Unstable crack propagation phase (phase III): where the increasing rate of the axial stress slightly dwindles. The AE counts exponentially boom as the stress rises, which infers that the storage of elastic energy is strong enough to trigger the eruption of an abundance of micro-cracks (Martin and Chandler 1994; Song et al. 2019; Zhang et al. 2020). In this phase, the variation of AIRT is dominated by the frictional heat effect and fracture effect. As stated by Liu et al. (2006), the generation of cracks (fracture effect) consumes the energy, which will further reduce the AIRT. Contrarily, the friction between cracks, joints, and grains generates much more heat, which, in turn, monotonically increases the AIRT. As shown in Fig. 7, the AIRT of all samples increases in this phase. This is attributed to the produced frictional heat energy compensating the dissipative energy used for crack initiation and propagation. Another reason is due to the fact that the crack initiates from the interior of rock rather than the surface, which postpones the decrease of the detected AIRT on rock surface.
4. Post-peak phase (phase IV): where the axial stress suddenly drops to zero accompanied by the majority of AE counts occurrence. In this phase, the AIRT variation of dry and saturated samples is markedly distinct, which will be further discussed in Sect. 3.5.

3.3 Thermal–Mechanical Response Before Peak Stress

Figure 8 plots the thermo-mechanical response of different rocks before peak stress. Generally, the variation of AIRT (ΔT) rises with the increase of uniaxial stress. During phase I, the variation of temperature shows a rapid rise. Afterwards, the increasing rate of AIRT variation seems to slightly decrease during phase II. This is likely due to the fact that the plastic deformation caused by the closure of initial defects will produce more heat. The stress at the turning point of the increasing rate of ΔT can be determined as the crack closure threshold.

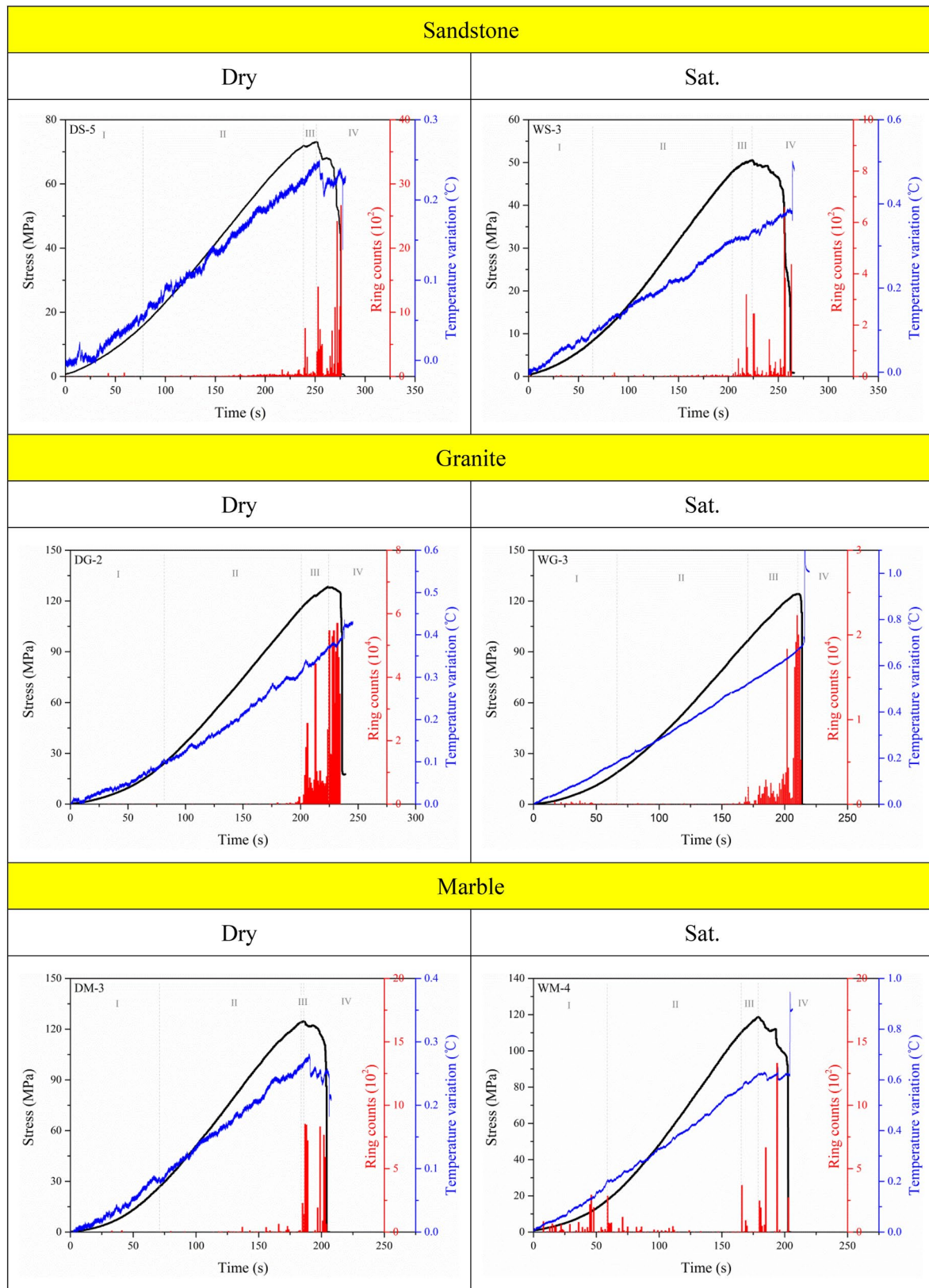


Fig. 7 Histories of axial stress, AE counts, and temperature variation versus time for different rock types under dry and saturated conditions

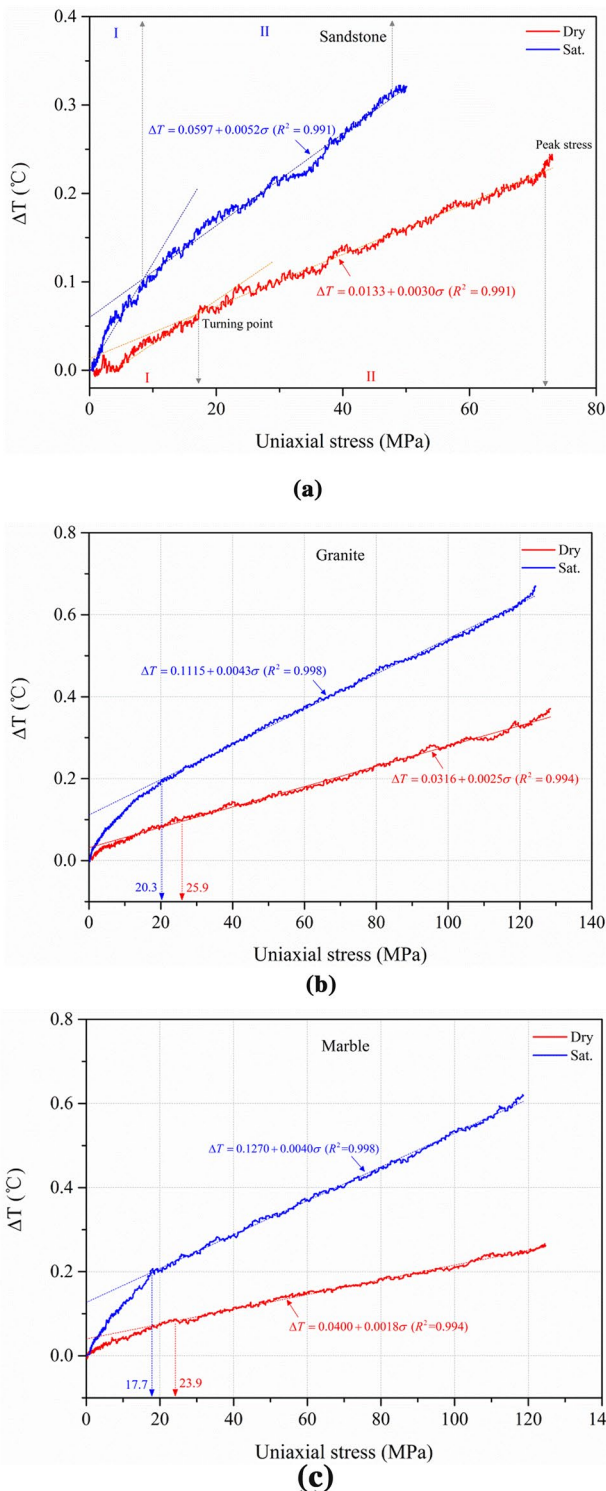


Fig. 8 Thermo-mechanical response of different rocks: **a** sandstone, **b** granite, and **c** marble

Figure 8 also illustrates that the variation in AIRT rises linearly with the uniaxial stress (σ) during the elastic deformation phase (phase II). This indicates that the thermal-elastic effect dominates the temperature increment. According to thermal-elastic theory (Wu et al. 2006b; Luong 2007), the variation of the IRR temperature of an isotropic-elastic solid is linearly related to the variation of the sum of principal stresses. Rock material is regarded as an elastic solid in this phase, so the relationship between σ versus ΔT could be expressed by the following function:

$$\Delta T = a\sigma + b, \tag{2}$$

where a and b are fitting constants. The fitting curves plotted in Fig. 8 is highly consistent with the testing data set, which indicates that ΔT increases versus stress with a constant rate. The slope a can be defined as the heating rate.

Figure 9 illustrates the average heating rate in the elastic deformation phase. Under dry state, the sandstone and granite samples hold a higher heating rate compared to the marble. This could be explained from different mineralogical compositions. As listed in Table 2, the sandstone and granite contain some relatively soft minerals, such as mica, smectite, and chlorite, in the former or muscovite and chlorite in the latter. The soft and ductile minerals hold a larger deformation compared to the hard grains under the same stress to generate more heat energy (Salami et al. 2017). However, the marble is mainly composed of the dolomite with high resistance. The stronger dolomite makes the IRR temperature of marble rises in a slighter pattern as the stress increases.

From Fig. 9, we can also clearly observe that the heating rates of the three rocks remarkably increase after water saturation. This indicates that the presence of water facilitates the release of thermal energy during elastic deformation. The potential mechanisms can be interpreted from the following viewpoints:

1. The softening of minerals: the deformation of ductile materials produces more heat compared with hard ones exposed to the same stress state (Vergani et al. 2014; Salami et al. 2017). Because of the water presence, physical weathering occurs for some minerals, especially swelling clay minerals (e.g., smectite) (Hawkins and McConnell 1992; Wasantha et al. 2018; Cai et al. 2019). This renders rock samples more ductile. This mechanism can be characterized by the water-induced reduction in elastic modulus (see Fig. 6). The elastic modulus of the sandstone holds the largest decline due to the highest content of smectite (Cai et al. 2019), while the drop for granite and marble is relatively gentle. Thus, this effect is not pronounced in the granite and marble.
2. Chemical reactions: some of the constituent minerals can chemically react with water under wet environment.

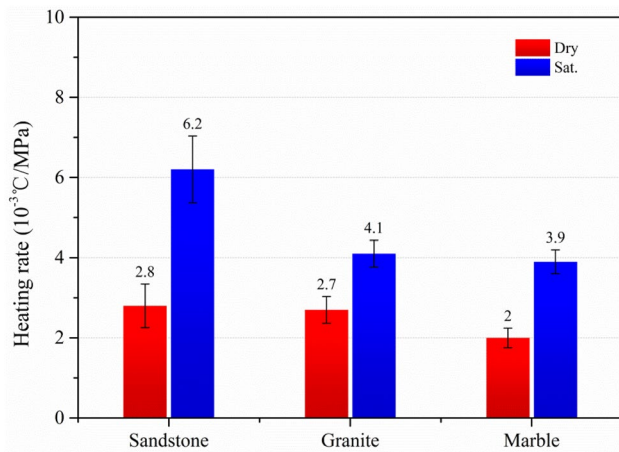
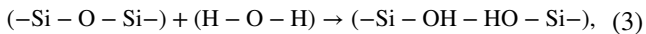
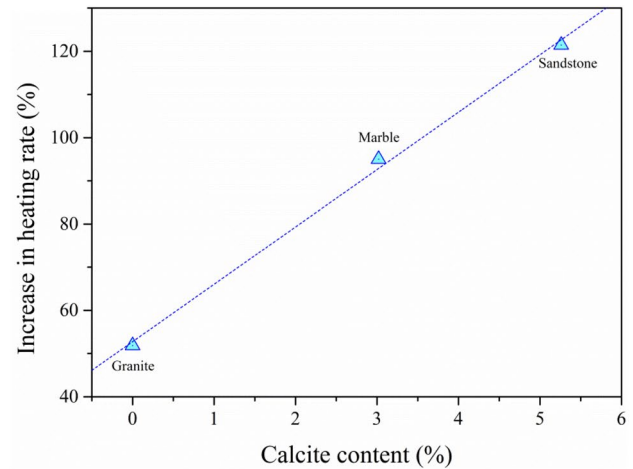


Fig. 9 Heating rate of dry and saturated rocks during elastic deformation phase

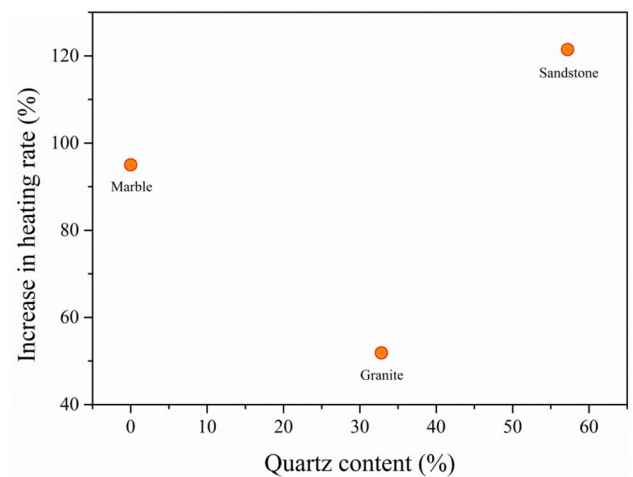
According to the mineral composition, two reactions, i.e., the hydrolysis of quartz (Eq. 3) (Atkinson and Meredith 1981; Eppes and Keanini 2017; Zhou et al. 2018c) and the dissolution of calcite (Eq. 4) (Ciantia et al. 2015; Liu et al. 2019b), are dominant as the following formulae:



Both of two reactions are exothermic due to the heat content of the products which is lower than that of the reactants (Bondi and Simkin 1956; Smith et al. 2004). Based on the second law of thermodynamics (Elliott and Lira 2007), the decrease in heat content of products must be compensated by releasing heat energy. In theory, the more quartz and calcite contained in rock, the more heat generated from chemical reactions. Figure 10 plots the relationship between the water-induced increase in heating rate and the content of quartz or calcite mineral. The increasing extent of heating rate linearly rises with the increase of calcite content (see Fig. 10a). However, the correlation between the increasing extent of heating rate and the calcite content is ambiguous, as shown in Fig. 10b. The heating rate increment of the granite containing considerable quartz content is exceptionally lower than that of the marble without quartz. The possible reason is that the calcite dissolution produces much more heat than quartz hydrolysis, although the content of calcite is tiny. The other reason is that the quartz of hydrolysis is limited. The quartz is soluble when the water can flow into the new-formed fracture tip zone (Atkinson and Meredith 1981). Cai et al. (2019) elucidated that the granite is tested under un-drained condition because of the extremely low



(a)



(b)

Fig. 10 Water-induced increase in heating rate versus the contents of **a** calcite and **b** quartz minerals

porosity while the sandstone under drained one. In other words, the water is unable to migrate freely in the granite sample, leading to a limited solution rate of quartz.

3. The increase of shear crack: Hawkins and McConnell (1992) compared the microscopic failure patterns of a large amount of rocks under dry and saturated conditions. They stated that the water presence triggers a transform from axial cleavage (tensile) in dry state into shear or a shear/tensile mixed mode due to the reduction in frictional coefficient at grain boundaries. On the microscopic scale, several researchers identified the crack type by means of acoustic emission method (Cai et al. 2019; Liu et al. 2019b; Yao et al. 2019). They discovered that the tensile crack is dominant under dry condition, while more shear cracks are observed in the water-saturated rock samples. The increasing shear

cracks result in more severe crack sliding to produce much more thermal energy.

To sum up, among the three rocks, the water-saturated sandstone exhibits the most drastic increase in terms of heating rate due to the coupled effects of mineral softening, chemical reactions, and increasing shear crack. The dissolution of calcite and the increase of shear crack lead to a moderate increase in the heating rate for the marble. The least increase in heating rate for the granite is attributed to the water-induced shear crack increase.

3.4 Water Saturation Effects on the AIRT Increment at Peak Stress

Figure 11 displays the AIRT increment at peak stress (ΔT_f) for dry and saturated rocks. Under dry condition, the granite samples hold the largest value of ΔT_f among the three rocks, followed by the marble and then the sandstone. It is clear that the ΔT_f of the three rocks dramatically rises after water saturation. This further proves that the presence of water promotes the release of heat energy of rock under compression. The increasing extent of the marble is the most remarkable, up to 114.0%, and those of the sandstone and the granite are 73.3% and 57.9%, respectively.

From Fig. 12, it is evident that the AIRT increment at peak stress not only depends on the moisture condition but also on the rock strength. The temperature increment at peak stress exhibits a linearly positive correlation with rock strength, i.e., it increases with the rise of rock strength under both dry and saturated conditions. The primary reason might be that the brittle rock with higher strength stores abundant strain energy before failure. More energy is potentially dissipated in a thermal manner. Consequently, the increase of rock strength rises the AIRT at failure.

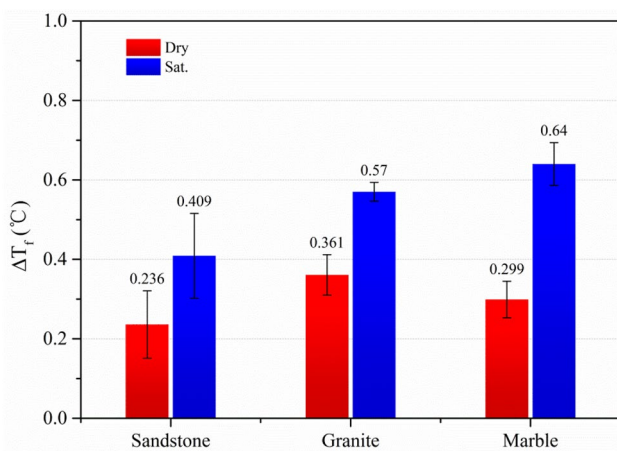


Fig. 11 AIRT increment at peak stress of dry and saturated rocks

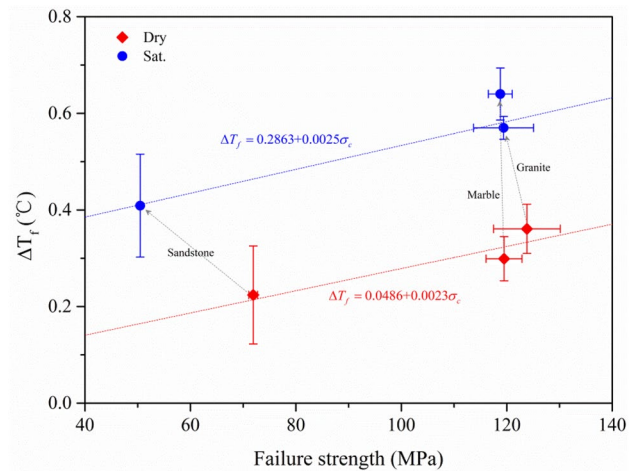


Fig. 12 AIRT increment at peak stress versus rock strength under dry and saturated conditions (the gray arrow line denotes saturated data)

3.5 Temperature Variation on Fractures

Figure 13 shows the spatial-temporal evolution of the IRR temperature of dry and saturated rocks under uniaxial compression. When the load level is low, the IRR temperature variation on sample surface is quite limited and evenly distributed. Afterwards, the overall temperature rises with the increase of external load. Interestingly, the temperature increment at bottom of sample is apparently higher than that at top. This is probably due to the frictional effect between the sample ends and the loading platen. Before peak stress is reached, no apparent temperature anomalies can be observed on the sample surfaces. This lends support to our hypothesis that crack initiates inside the rock rather than on the surface.

After peak stress, the AIRT variation of rocks violently fluctuates with the decrease of uniaxial stress. The temperature variation depends on the competition between the heat produced by the frictional effect and the heat dissipation caused by the stress decline and the fracture effect. Soon after, surface fragments spall from the rock body. The new-formed fractures with high temperature emerge in the view of the IR thermographic camera, resulting in the abrupt change of temperature. This means that the temperature inside rock is greater than that on rock surface due to the severe frictional effect. At this time, the mean value of the temperature variation in the ZOI is not appropriate for characterizing the temperature increment inside the rock, because the fracture surface area for each sample appearing in the ZOI is different. Hence, we measured the maximum temperature increment (ΔT_{max}) in the final frame of IRR image to characterize the temperature variation inside the rock.

Figure 14 illustrates the maximum temperature increment on fracture surface of dry and saturated rocks. Apparently, the presence of water increases the ΔT_{max} on fracture

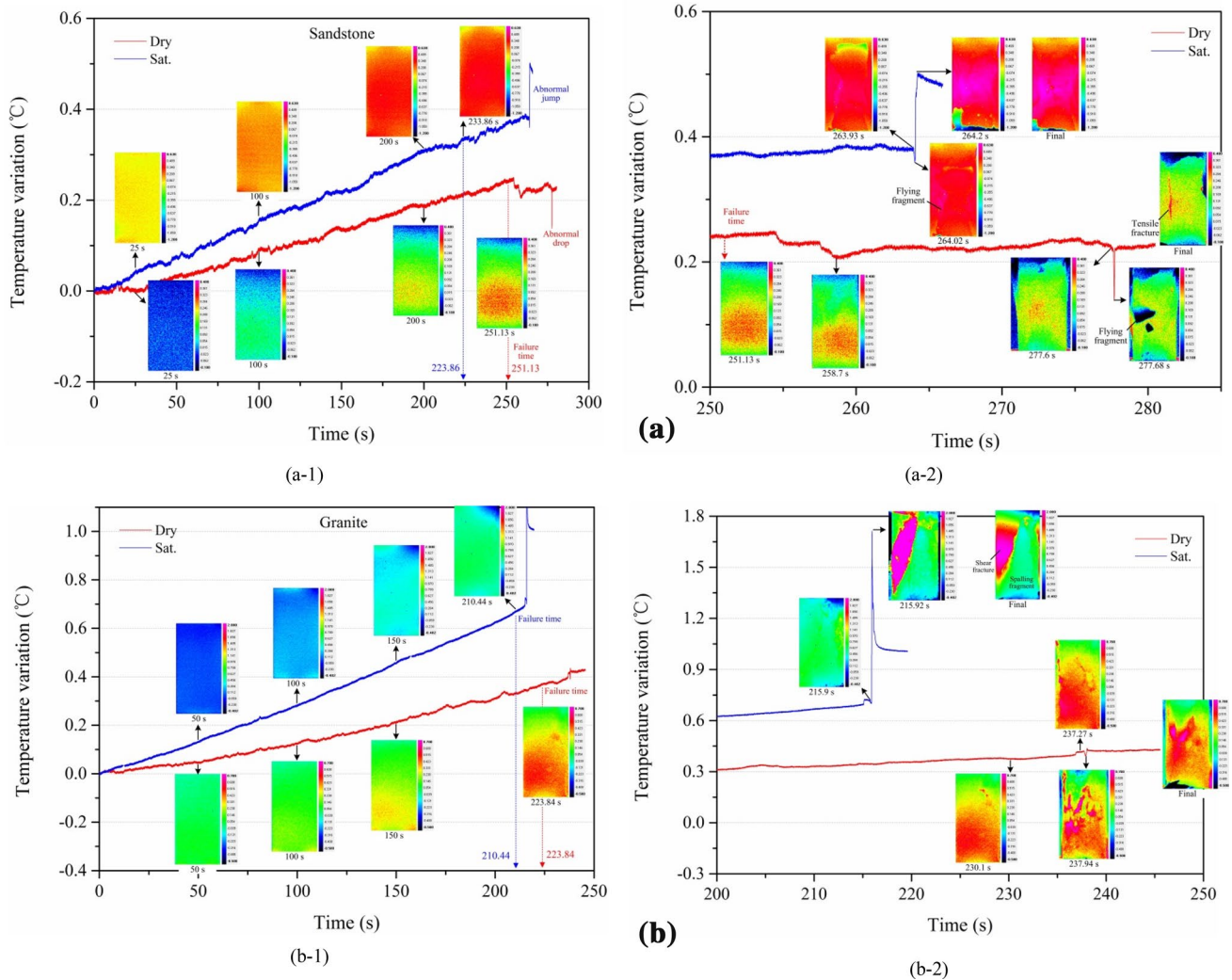


Fig. 13 Evolution of temperature variation and IRR images: **a** sandstone, **b** granite, and **c** marble (figures in the left column represent the overall history of temperature variation, and those in the right column show the temperature variation in post peak)

surface. For the final circumstance, the uniaxial stress drops zero. The thermo-elastic effect is absent due to the stress relaxation. Therefore, the temperature increment of fracture surface is controlled by the fracture effect and the frictional heat effect. On one hand, the water decreases the number of crack creation, this will be reflected by the cumulative ring counts (see Table 4). Moreover, as reported by Zang et al. (1996) and Li et al. (2019), the trans-granular fracture frequently occurs in dry rocks, while the inter-granular fracture commonly happens in saturated rocks probably as a consequence of the reduced grain boundary friction. They render the less energy dissipation in the fracture of saturated rocks. On the other hand, more heat generated from the crack sliding due to the increasing shear cracks during the failure of saturated samples. These two factors dominantly lead to the increase in ΔT_{\max} of rock fracture after water saturation.

4 Summary and Conclusions

To study the water saturation effects on the thermal IRR characteristics of rocks and reveal the water sensitivity of different rock types, three representative rocks (sandstone, granite, and marble) were selected for tests. Uniaxial compression tests were conducted on oven-dried and water-saturated rock samples. Water-induced variations of their mechanical parameters and AE features were captured. An infrared thermographic camera was applied to monitor and record the evolution of IRR temperature during the whole loading process. The relation between the AIRT variation and the applied stress was obtained. The changes in IRR temperature features due to water saturation such as the heating rate in elastic deformation phase, the temperature increment at peak stress, and the maximum temperature in

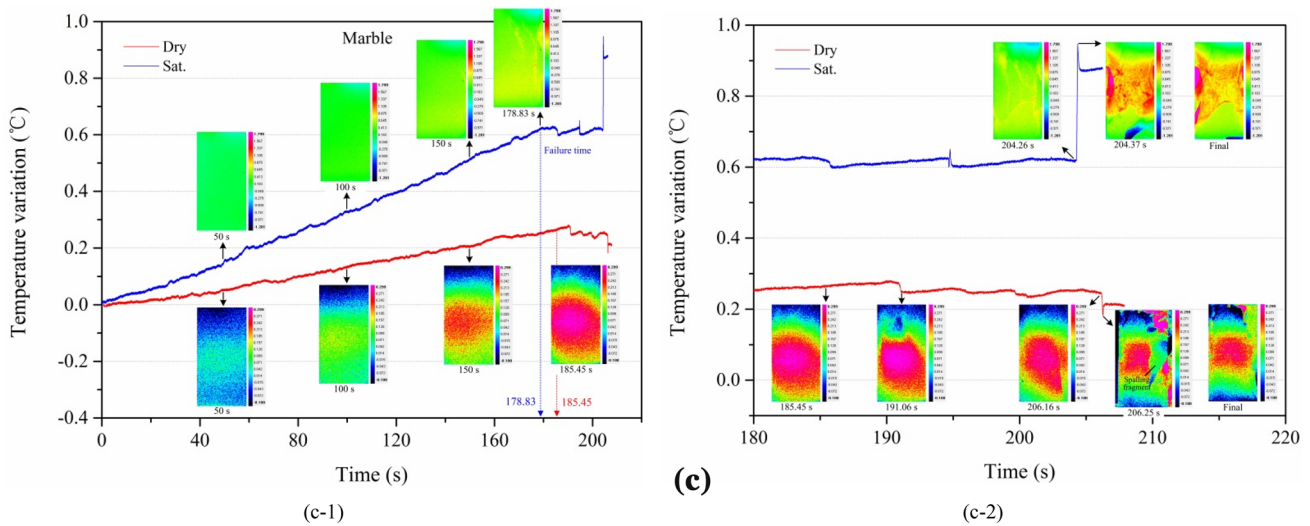


Fig. 13 (continued)

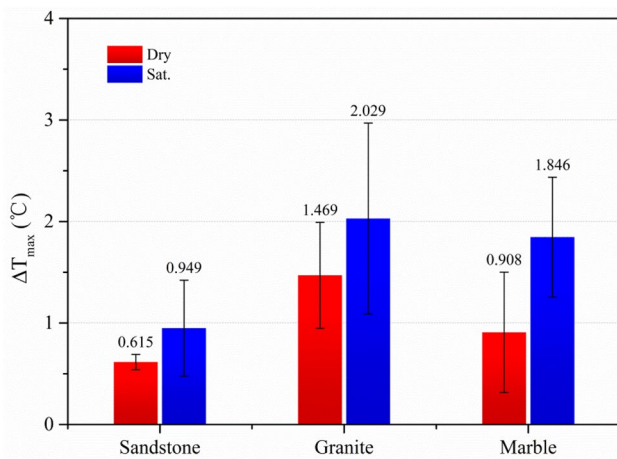


Fig. 14 The max temperature increment on fracture surface of dry and saturated rocks

the fracture surface were analyzed. The main conclusions of this research are summarized as follows:

1. The presence of water weakens the mechanical properties (including UCS, elastic modulus, and critical strain) of rocks in different extents. Among the three tested rocks, the mechanical parameters for the sandstone are the most susceptible to water, and then followed by the granite and the marble.
2. For a given rock type, the surface AIRT of saturated samples is significantly higher than that of dry ones under the same stresses. This indicates that water promotes the release of heat energy within rocks under uniaxial de-

mation, which further leads to the increase in the heating rate in elastic deformation phase, the AIRT increment at peak stress, as well as the temperature on the new-formed fracture surface.

3. During elastic deformation phase, the water-induced increase in heating rate primarily depends on the mineralogy and secondly on the porosity. For water-saturated condition, the joint effects of mineral softening, chemical reactions, and increasing shear cracks are responsible for the most considerable increase of the heating rate for the sandstone. A moderate increase in heating rate for the marble is mainly induced by calcite dissolution and the increase of shear crack. For the granite, the mineral softening and calcite dissolution effects do not work anymore due to the absence of swelling clay minerals and calcite. The quartz hydrolysis is also limited by the low porosity. Consequently, only the effect of increasing shear crack slightly enhances the heating rate.

4. Besides the moisture state, the UCS of rock also affects the AIRT increment at peak stress. Under both dry and saturated conditions, the AIRT increment at peak stress shows a linearly positive correlation versus UCS.

5. The present research suggests that water plays an important role in controlling the thermal IRR features of rock materials. However, the tested rocks are limited to hard brittle ones. Similar tests will be further conducted on other rock types, such as coal, limestone, mudstone, and shale to testify whether these findings are more generally applicable.

Acknowledgements The work is supported by financial grants from the National Basic Research Program of China (2015CB060200), the National Natural Science Foundation of China (41772313), the Natural Science Foundation of Hunan (2015JJ4067), and the Graduated Students' Research and Innovation Fund Project of Central South University (2018zsts210). The authors are very grateful to the financial contribution and convey their appreciation for supporting this basic research. The authors also wish to thank Mr. Yizhong Luo from the Advanced Research Center, Central South University for his help in experiments.

Compliance with Ethical Standards

Conflict of interest The authors declare that they have no conflict of interest.

References

- Atkinson BK, Meredith PG (1981) Stress corrosion cracking of quartz: a note on the influence of chemical environment. *Tectonophysics* 77:T1–T11. [https://doi.org/10.1016/0040-1951\(81\)90157-8](https://doi.org/10.1016/0040-1951(81)90157-8)
- Bian K, Liu J, Zhang W et al (2019) Mechanical behavior and damage constitutive model of rock subjected to water-weakening effect and uniaxial loading. *Rock Mech Rock Eng*. <https://doi.org/10.1007/s00603-018-1580-4>
- Boltzmann L (1884) Ableitung des Stefan'schen Gesetzes, betreffend die Abhängigkeit der Wärmestrahlung von der Temperatur aus der electromagnetischen Lichttheorie. *Ann Phys* 258:291–294. <https://doi.org/10.1002/andp.18842580616>
- Bondi A, Simkin DJ (1956) On the hydrogen bond contribution to the heat of vaporization of aliphatic alcohols. *J Chem Phys* 25:1073–1074. <https://doi.org/10.1063/1.1743102>
- Brady BT, Rowell GA (1986) Laboratory investigation of the electro-dynamics of rock fracture. *Nature* 321:488–492. <https://doi.org/10.1038/321488a0>
- Cai X, Zhou Z, Du X, Zang H (2019) Water-weakening effects on the mechanical behavior of different rock types: phenomena and mechanisms. *Appl Sci* 9:4450. <https://doi.org/10.3390/app9204450>
- Cai X, Zhou Z, Du X (2020) Water-induced variations in dynamic behavior and failure characteristics of sandstone subjected to simulated geo-stress. *Int J Rock Mech Min Sci* 130:104339. <https://doi.org/10.1016/j.ijrmmms.2020.104339>
- Cheng F, Li Z, Li G et al (2018) Influence of prefabricated fissure angle on sandstone damage and infrared radiation temperature characteristics. *J Geophys Eng*. <https://doi.org/10.1088/1742-2140/aaacaf>
- Ciantia MO, Castellanza R, Crosta GB, Hueckel T (2015) Effects of mineral suspension and dissolution on strength and compressibility of soft carbonate rocks. *Eng Geol* 184:1–18. <https://doi.org/10.1016/j.enggeo.2014.10.024>
- Cong L, Zhang Y, Xiao F, Wei Q (2016) Laboratory and field investigations of permeability and surface temperature of asphalt pavement by infrared thermal method. *Constr Build Mater*. <https://doi.org/10.1016/j.conbuildmat.2016.03.078>
- Dang W, Wu W, Konietzky H, Qian J (2019) Effect of shear-induced aperture evolution on fluid flow in rock fractures. *Comput Geotech* 114:103152. <https://doi.org/10.1016/j.compgeo.2019.103152>
- Du K, Li XB, Li DY, Weng L (2015) Failure properties of rocks in true triaxial unloading compressive test. *Trans Nonferrous Met Soc China* 25:571–581. [https://doi.org/10.1016/S1003-6326\(15\)63639-1](https://doi.org/10.1016/S1003-6326(15)63639-1) (English Ed)
- Elliott JR, Lira CT (2007) Introductory chemical engineering thermodynamics. 2nd edn. Prentice Hall
- Eppes MC, Keanini R (2017) Mechanical weathering and rock erosion by climate-dependent subcritical cracking. *Rev Geophys* 55:470–508. <https://doi.org/10.1002/2017RG000557>
- Hawkins AB, McConnell BJ (1992) Sensitivity of sandstone strength and deformability to changes in moisture content. *Q J Eng Geol Hydrogeol* 25:115–130. <https://doi.org/10.1144/GSL.QJEG.1992.025.02.05>
- He M, Jia X, Gong W, Faramarzi L (2010) Physical modeling of an underground roadway excavation in vertically stratified rock using infrared thermography. *Int J Rock Mech Min Sci* 47:1212–1221. <https://doi.org/10.1016/j.ijrmmms.2010.06.020>
- Jia H, Zi F, Yang G et al (2019) Influence of pore water (ice) content on the strength and deformability of Frozen Argillaceous Siltstone. *Rock Mech Rock Eng*. <https://doi.org/10.1007/s00603-019-01943-0>
- Jiang Q, Cui J, Feng X, Jiang Y (2014) Application of computerized tomographic scanning to the study of water-induced weakening of mudstone. *Bull Eng Geol Environ* 73:1293–1301. <https://doi.org/10.1007/s10064-014-0597-5>
- Li Z, Yin S, Niu Y et al (2018) Experimental study on the infrared thermal imaging of a coal fracture under the coupled effects of stress and gas. *J Nat Gas Sci Eng* 55:444–451. <https://doi.org/10.1016/j.jngse.2018.05.019>
- Li H, Shen R, Li D, et al (2019) Acoustic emission multi-parameter analysis of dry and saturated sandstone with cracks under uniaxial compression. *Energies* 12(10):1959. <https://doi.org/10.3390/en12101959>
- Liu S, Wu L, Wu Y (2006) Infrared radiation of rock at failure. *Int J Rock Mech Min Sci* 43:972–979. <https://doi.org/10.1016/j.ijrmmms.2005.12.009>
- Liu X, Liang Z, Zhang Y et al (2018) Experimental study on the monitoring of rockburst in tunnels under dry and saturated conditions using AE and infrared monitoring. *Tunn Undergr Sp Technol* 82:517–528. <https://doi.org/10.1016/j.tust.2018.08.011>
- Liu B, Yang H, Karekal S (2019a) Effect of water content on argillization of mudstone during the tunnelling process. *Rock Mech Rock Eng*. <https://doi.org/10.1007/s00603-019-01947-w>
- Liu X, Wu L, Zhang Y et al (2019b) Frequency properties of acoustic emissions from the dry and saturated rock. *Environ Earth Sci* 78:67. <https://doi.org/10.1007/s12665-019-8058-x>
- Lou Q, He X (2018) Experimental study on infrared radiation temperature field of concrete under uniaxial compression. *Infrared Phys Technol* 90:20–30. <https://doi.org/10.1016/j.infrared.2018.01.033>
- Luong MP (2007) Introducing infrared thermography in soil dynamics. *Infrared Phys Technol* 49:306–311. <https://doi.org/10.1016/j.infrared.2006.06.025>
- Luong MP, Emami M (2013) Characterization of mechanical damage in granite. *Fract Struct Integr* 27:38–42. <https://doi.org/10.3221/IGF-ESIS.27.05>
- Ma L, Sun H (2018) Spatial-temporal infrared radiation precursors of coal failure under uniaxial compressive loading. *Infrared Phys Technol* 93:144–153. <https://doi.org/10.1016/j.infrared.2018.07.034>
- Ma LQ, Li QQ, Cao XQ, Zhou T (2013) Variation characteristics of internal infrared radiation temperature of coal-rock mass in compression process. *J China Univ Min Technol* 42:331–336. <https://doi.org/10.13247/j.cnki.jcumat.2013.03.001>
- Ma L, Sun H, Zhang Y et al (2016) Characteristics of infrared radiation of coal specimens under uniaxial loading. *Rock Mech Rock Eng* 49:1567–1572. <https://doi.org/10.1007/s00603-015-0780-4>
- Ma D, Duan H, Li X et al (2019a) Effects of seepage-induced erosion on nonlinear hydraulic properties of broken red sandstones. *Tunn Undergr Sp Technol* 91:102993. <https://doi.org/10.1016/j.tust.2019.102993>

- Ma D, Wang J, Cai X et al (2019b) Effects of height/diameter ratio on failure and damage properties of granite under coupled bending and splitting deformation. *Eng Fract Mech* 220:106640. <https://doi.org/10.1016/j.engfracmech.2019.106640>
- Ma L, Zhang Y, Cao K, Wang Z (2019c) An experimental study on infrared radiation characteristics of sandstone samples under uniaxial loading. *Rock Mech Rock Eng*. <https://doi.org/10.1007/s00603-018-1688-6>
- Martelli G, Smith PN, Woodward AJ (1989) Light, radiofrequency emission and ionization effects associated with rock fracture. *Geophys J Int* 98:397–401. <https://doi.org/10.1111/j.1365-246X.1989.tb03362.x>
- Martin CD, Chandler NA (1994) The progressive fracture of Lac du Bonnet granite. *Int J Rock Mech Min Sci* 31:643–659. [https://doi.org/10.1016/0148-9062\(94\)90005-1](https://doi.org/10.1016/0148-9062(94)90005-1)
- Mineo S, Pappalardo G (2016) The use of infrared thermography for porosity assessment of intact rock. *Rock Mech Rock Eng* 49:3027–3039. <https://doi.org/10.1007/s00603-016-0992-2>
- Mineo S, Pappalardo G (2019) InfraRed Thermography presented as an innovative and non-destructive solution to quantify rock porosity in laboratory. *Int J Rock Mech Min Sci* 115:99–110. <https://doi.org/10.1016/j.ijrmms.2019.01.012>
- Minh Phono Luong (1990) Infrared thermovision of damage processes in concrete and rock. *Eng Fract Mech* 35:291–301. [https://doi.org/10.1016/0013-7944\(90\)90207-W](https://doi.org/10.1016/0013-7944(90)90207-W)
- Pappalardo G, Mineo S, Angrisani AC et al (2018) Combining field data with infrared thermography and DInSAR surveys to evaluate the activity of landslides: the case study of Randazzo Landslide (NE Sicily). *Landslides* 15:2173–2193. <https://doi.org/10.1007/s10346-018-1026-9>
- Peng K, Zhou J, Zou Q et al (2019) Effects of stress lower limit during cyclic loading and unloading on deformation characteristics of sandstones. *Constr Build Mater*. <https://doi.org/10.1016/j.conbuildmat.2019.04.183>
- Ren R, Han K, Zhao P et al (2019) Identification of asphalt fingerprints based on ATR-FTIR spectroscopy and principal component-linear discriminant analysis. *Constr Build Mater* 198:662–668. <https://doi.org/10.1016/j.conbuildmat.2018.12.009>
- Salami Y, Dano C, Hicher PY (2017) Infrared thermography of rock fracture. *Géotechnique Lett* 7:1–5. <https://doi.org/10.1680/jgele.16.00131>
- Saraf AK, Rawat V, Banerjee P et al (2008) Satellite detection of earthquake thermal infrared precursors in Iran. *Nat Hazards* 47:119–135. <https://doi.org/10.1007/s11069-007-9201-7>
- Seo H, Choi H, Park J et al (2017) Crack detection in pillars using infrared thermographic imaging. *Geotech Test J* 40:20150245. <https://doi.org/10.1520/GTJ20150245>
- Sheinin VI, Blokhin DI (2012) Features of thermomechanical effects in rock salt samples under uniaxial compression. *J Min Sci* 48:39–45. <https://doi.org/10.1134/s1062739148010054>
- Smith JD, Cappa CD, Wilson KR et al (2004) Energetics of hydrogen bond network rearrangements in liquid water. *Science* (80–) 306:851–853. <https://doi.org/10.1126/science.1102560>
- Song Z, Frühwirth T, Konietzky H (2018) Characteristics of dissipated energy of concrete subjected to cyclic loading. *Constr Build Mater*. <https://doi.org/10.1016/j.conbuildmat.2018.02.076>
- Song Z, Konietzky H, Herbst M (2019) Three-dimensional particle model based numerical simulation on multi-level compressive cyclic loading of concrete. *Constr Build Mater*. <https://doi.org/10.1016/j.conbuildmat.2019.07.260>
- Song Z, Frühwirth T, Konietzky H (2020) Inhomogeneous mechanical behaviour of concrete subjected to monotonic and cyclic loading. *Int J Fatigue*. <https://doi.org/10.1016/j.ijfatigue.2019.105383>
- Sun H, Ma L, Adeleke N, Zhang Y (2017a) Background thermal noise correction methodology for average infrared radiation temperature of coal under uniaxial loading. *Infrared Phys Technol* 81:157–165. <https://doi.org/10.1016/j.infrared.2017.01.001>
- Sun X, Xu H, He M, Zhang F (2017b) Experimental investigation of the occurrence of rockburst in a rock specimen through infrared thermography and acoustic emission. *Int J Rock Mech Min Sci* 93:250–259. <https://doi.org/10.1016/j.ijrmms.2017.02.005>
- Tang SB, Yu CY, Heap MJ et al (2018) The influence of water saturation on the short- and long-term mechanical behavior of red sandstone. *Rock Mech Rock Eng*. <https://doi.org/10.1007/s00603-018-1492-3>
- Vergani L, Colombo C, Libonati F (2014) A review of thermographic techniques for damage investigation in composites. *Frat ed Integrata Strutt* 8:1–12. <https://doi.org/10.3221/IGF-ESIS.27.01>
- Wang C, Lu Z, Liu L et al (2016) Predicting points of the infrared precursor for limestone failure under uniaxial compression. *Int J Rock Mech Min Sci* 88:34–43. <https://doi.org/10.1016/j.ijrmms.2016.07.004>
- Wasantha PLP, Ranjith PG, Permata G, Bing D (2018) Damage evolution and deformation behaviour of dry and saturated sandstones: insights gleaned from optical measurements. *Meas J Int Meas Confed* 130:8–17. <https://doi.org/10.1016/j.measurement.2018.07.075>
- Weng L, Wu Z, Liu Q, Wang Z (2019) Energy dissipation and dynamic fragmentation of dry and water-saturated siltstones under sub-zero temperatures. *Eng Fract Mech* 220:106659. <https://doi.org/10.1016/j.engfracmech.2019.106659>
- Wong LNY, Maruvanchery V, Liu G (2016) Water effects on rock strength and stiffness degradation. *Acta Geotech* 11:713–737. <https://doi.org/10.1007/s11440-015-0407-7>
- Wu L, Wang J (1998) Infrared radiation features of coal and rocks under loading. *Int J Rock Mech Min Sci* 35:969–976. [https://doi.org/10.1016/S0148-9062\(98\)00007-2](https://doi.org/10.1016/S0148-9062(98)00007-2)
- Wu L, Cui C, Geng N, Wang J (2000) Remote sensing rock mechanics (RSRM) and associated experimental studies. *Int J Rock Mech Min Sci* 37:879–888. [https://doi.org/10.1016/S1365-1609\(99\)00066-0](https://doi.org/10.1016/S1365-1609(99)00066-0)
- Wu L, Liu S, Wu Y, Wu H (2002) Changes in infrared radiation with rock deformation. *Int J Rock Mech Min Sci* 39:825–831. [https://doi.org/10.1016/S1365-1609\(02\)00049-7](https://doi.org/10.1016/S1365-1609(02)00049-7)
- Wu L, Wu Y, Liu S et al (2004) Infrared radiation of rock impacted at low velocity. *Int J Rock Mech Min Sci* 41:321–327. [https://doi.org/10.1016/S1365-1609\(03\)00099-6](https://doi.org/10.1016/S1365-1609(03)00099-6)
- Wu L, Liu S, Wu Y, Wang C (2006a) Precursors for rock fracturing and failure—Part I: IRR image abnormalities. *Int J Rock Mech Min Sci* 43:473–482. <https://doi.org/10.1016/j.ijrmms.2005.09.002>
- Wu L, Liu S, Wu Y, Wang C (2006b) Precursors for rock fracturing and failure—Part II: IRR T-Curve abnormalities. *Int J Rock Mech Min Sci* 43:483–493. <https://doi.org/10.1016/j.ijrmms.2005.09.001>
- Xiao F, He J, Liu Z et al (2019) Analysis on warning signs of damage of coal samples with different water contents and relevant damage evolution based on acoustic emission and infrared characterization. *Infrared Phys Technol* 97:287–299. <https://doi.org/10.1016/j.infrared.2019.01.007>
- Yang D, Chanchole S, Valli P, Chen L (2013) Study of the anisotropic properties of argillite under moisture and mechanical loads. *Rock Mech Rock Eng* 46:247–257. <https://doi.org/10.1007/s00603-012-0267-5>
- Yao H, You Z, Li L et al (2013) Rheological properties and chemical analysis of nanoclay and carbon microfiber modified asphalt with Fourier transform infrared spectroscopy. *Constr Build Mater* 38:327–337. <https://doi.org/10.1016/j.conbuildmat.2012.08.004>
- Yao Q, Chena T, Tang C et al (2019) Influence of moisture on crack propagation in coal and its failure modes. *Eng Geol* 258:2019
- Zang A, Wagner CF, Dresen G (1996) Acoustic emission, microstructure, and damage model of dry and wet sandstone stressed

- to failure. *J Geophys Res Solid Earth* 101:17507–17521. <https://doi.org/10.1029/96jb01189>
- Zhang YB, Bin CB, Jing GH (2012) The research of water effect on infrared radiation of concrete failure process. *Appl Mech Mater* 256–259:2754–2759. <https://doi.org/10.4028/www.scientific.net/AMM.256-259.2754>
- Zhang GK, Li HB, Wang MY, Li XF (2020) Crack initiation of granite under uniaxial compression tests: a comparison study. *J Rock Mech Geotech Eng*. <https://doi.org/10.1016/j.jrmge.2019.07.014>
- Zhao Y, Jiang Y (2010) Acoustic emission and thermal infrared precursors associated with bump-prone coal failure. *Int J Coal Geol* 83:11–20. <https://doi.org/10.1016/j.coal.2010.04.001>
- Zhao Z, Yang J, Zhang D, Peng H (2017) Effects of wetting and cyclic wetting-drying on tensile strength of sandstone with a low clay mineral content. *Rock Mech Rock Eng* 50:485–491. <https://doi.org/10.1007/s00603-016-1087-9>
- Zheng YL, Zhang QB, Zhao J (2017) Effect of microwave treatment on thermal and ultrasonic properties of gabbro. *Appl Therm Eng* 127:359–369. <https://doi.org/10.1016/j.appltherm.2017.08.060>
- Zhou Z, Cai X, Cao W et al (2016) Influence of water content on mechanical properties of rock in both saturation and drying processes. *Rock Mech Rock Eng* 49:3009–3025. <https://doi.org/10.1007/s00603-016-0987-z>
- Zhou Z, Cai X, Ma D et al (2018a) Dynamic tensile properties of sandstone subjected to wetting and drying cycles. *Constr Build Mater* 182:215–232. <https://doi.org/10.1016/j.conbuildmat.2018.06.056>
- Zhou Z, Cai X, Ma D et al (2018b) Effects of water content on fracture and mechanical behavior of sandstone with a low clay mineral content. *Eng Fract Mech* 193:47–65. <https://doi.org/10.1016/j.engfracmech.2018.02.028>
- Zhou Z, Cai X, Ma D et al (2019) Water saturation effects on dynamic fracture behavior of sandstone. *Int J Rock Mech Min Sci* 114:46–61. <https://doi.org/10.1016/j.ijrmms.2018.12.014>
- Zhou Z, Zhou J, Cai X et al (2020) Acoustic emission source location considering refraction in layered media with cylindrical surface. *Trans Nonferrous Met Soc China*. [https://doi.org/10.1016/S1000-6326\(20\)65254-2](https://doi.org/10.1016/S1000-6326(20)65254-2) (English Ed)

Publisher's Note Springer Nature remains neutral with regard to jurisdictional claims in published maps and institutional affiliations.